PHYSICAL REVIEW A **81**, 063832 (2010)

Intense nonclassical light: Controllable two-photon Talbot effect

C. H. Raymond Ooi[1,2,*] and Boon Leong Lan[2]
[1]*Department of Physics, University of Malaya, 50603 Kuala Lumpur, Malaysia*
[2]*School of Engineering, Monash University, 46150 Bandar Sunway, Selangor, Malaysia*

(Received 9 February 2010; published 28 June 2010)

We study the spatial interference pattern of two-photon correlation function for a coherently phased linear array of N emitters with a double-Raman scheme, each producing nonclassically correlated photon pairs. The N^2 dependence in the two-photon correlation serves as a coherent amplification method for producing intense nonclassical light. The spatial distribution of the correlation can be controlled by lasers, and depends on the detection configuration. For two coincident detectors, the nonclassical correlation displays the spatial Talbot pattern, but modulated by quantum interference effect. The image revival distance is found to be twice the usual Talbot length. For symmetrically located detectors ($X_1 = -X_2$), the correlation displays a distorted Talbot pattern with intricate features and lack of symmetry.

DOI: 10.1103/PhysRevA.81.063832 PACS number(s): 42.50.Ar, 42.50.St

I. INTRODUCTION

Nonclassical light source is generated artificially and does not exist in nature. Recently, it was found that correlated photon pairs can provide optical resolution beyond the diffraction limit through coincident photon detection [1] and have been proposed for quantum imaging [2]. The photon pairs can also enhance the spectral resolution of atoms and molecules [3]. Particles with the double-Raman scheme can produce photon pairs with nonclassical properties, such as photon antibunching [4] in the correlation function $G^{(2)}$. The nonclassicality of photon pairs is also found in the two-atoms case [5]. In the many-atoms case or extended medium [6] the correlation function violates the Cauchy-Schwarz inequality. The results for extended medium are based on full quantum theory and agree with the experiment [7]. However, its applicability is limited to photon pairs at moderate intensity. Nonclassical light at high intensity has not been thoroughly studied both experimentally and theoretically. A sufficiently bright source of nonclassically correlated photons could become a new tool in optics. Several research groups claimed to have successfully produced nonclassical light sources with high brightness. Photonic crystal fiber [8] can generate up to 10^7 photon pairs per second, 100 times higher compared to laser-cooled atoms. The corresponding quantum theory was developed by Agrawal [9], valid for moderately high intensity. Recently, Harris proposed a scheme to generate single-cycle photon pairs [10] from periodic structure with nonlinear optics.

The quest toward intense nonclassical light source motivates our present work to study photon correlation for an array of quantum emitters. Coherently phased emissions can produce intensity that scales quadratically with the number of emitters in linear as well as circular configuration [11]. An interesting question follows: Would such scaling apply for correlated or joint coincident detection of nonclassically correlated photons? It is interesting to investigate how the interference pattern repeats regularly with the distance from the emitters, the Talbot effect [12]. Recently, the effect was found in waveguide modes [13], in terms of Wigner function [14], and in atomic systems [15]. The effect has been used in laser phase locking and incorporated into high-field laser systems [16]. More exotic applications of the effect include factorization of large numbers and evaluation of the Gauss sum [17]. Here, we will study how the nonclassicality of correlated photons affects the Talbot pattern for arrayed emitters. We analyze the spatial structure of the two-photon correlation from the array of emitters (see Fig. 1).

In Sec. II, two-photon amplitude for multiple double-Raman emitters is obtained from the amplitude for a single emitter. In Sec. III, we consider a particular case of a one-dimensional (1D) array within the paraxial approximation. Two possible detection schemes are considered in Sec. IV, each producing entirely different spatial structures. In the final Sec. V, we discuss the features and the implications of the obtained results.

II. NONCLASSICAL CORRELATION FOR MULTIPLE EMITTERS

We now consider an array of N quantum emitters (atoms or quantum dots), each located in periodic sites, with the distance between two emitters larger than an optical wavelength such that they are noninteracting, as shown in Fig. 1. Otherwise, dipole-dipole interaction due to proximity may contribute to the coherent effects [18]. Each emitter has three levels driven coherently by two lasers forming the double-Raman scheme [Fig. 1(a)]. The pump laser (with Rabi frequency Ω_p) creates the Stokes photon with wave vector $\mathbf{k}$ via an off-resonant Raman transition from level c to level b which is resonantly coupled by the control laser Ω_c to level a, creating the anti-Stokes photon with wave vector $\mathbf{q}$ [19]. For atoms, Rb-87 can be used, with the levels a,b,c corresponding to $|5^2P_{1/2}, F=1\rangle, |5^2S_{1/2}, F=2\rangle, |5^2S_{1/2}, F=1\rangle$, respectively (D1 transition). For quantum dots, the upper level corresponds to the biexciton XX which is coupled to two (intermediate) exciton levels X_1 and X_2, split by the exchange interaction due to anisotropy of the exciton wave function [see Fig 1(a)].

In order to study the interference effects of the two sequential detection of the Stokes and anti-Stokes photons [at $(\mathbf{r}_1,t_1)$ and at $(\mathbf{r}_2,t_2)$, respectively], we compute the two-photon correlation function $G^{(2)} = \langle\Psi|\hat{E}^{(-)}(\mathbf{r}_1,t_1)$

---

[*] bokooi73@yahoo.com

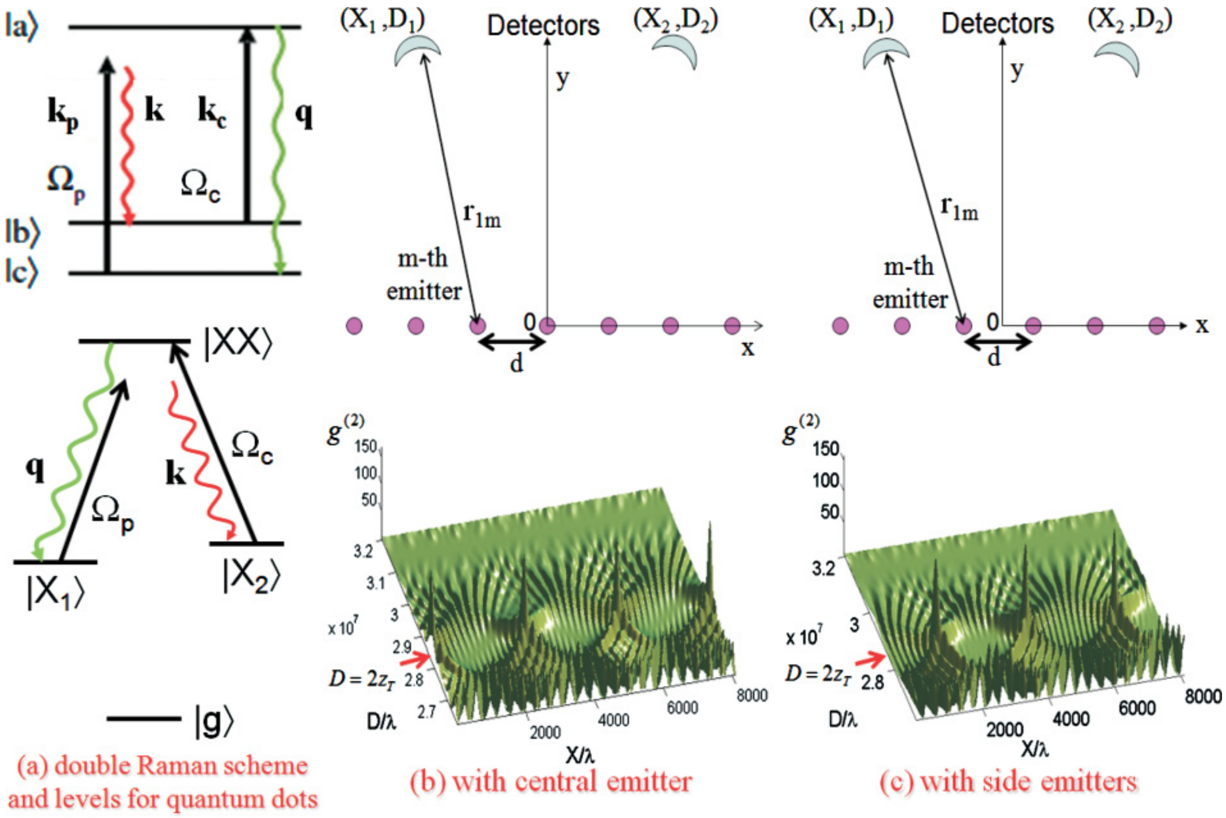

FIG. 1. (Color online) An array of quantum emitters, each producing correlated photons from the double-Raman scheme (inside orange frame). (a) Double-Raman scheme, applied to a typical scheme in quantum dots, (b) array with central emitters ($N = 31$) and the $g^{(2)}$ distribution, and (c) array with side emitters ($N = 30$) and the $g^{(2)}$. Note that the peaks in the images occur at $D = 2z_T = 4d^2/\lambda$ (nonclassical Talbot length) which is twice the classical length $z_T = \frac{2d^2}{\lambda}$. We use $X_2 = X_1$, $\Omega_c = 2000\Gamma$, $D_2 = 1.001D_1$, and $d = 3N^2\lambda$ with $\Gamma = 10^8$ s^{-1} and $\lambda = 0.3$ μm. Thus, the peaks emerge around $D/\lambda = 36N^4 = 2.9 \times 10^7$. All subsequent figures below are for case (a).

$\hat{E}^{(-)}(\mathbf{r}_2,t_2)\hat{E}^{(+)}(\mathbf{r}_2,t_2)\hat{E}^{(+)}(\mathbf{r}_1,t_1)|\Psi\rangle$. The Schrödinger equation approach for the single m-th atom with the double-Raman scheme located at $\mathbf{r}_m$ gives the analytical expression for the two-photon amplitude in the far field [20],

$$\psi_m^{(2)}(1,2) = \langle 0|\hat{E}^{(+)}(\mathbf{r}_2,t_2)\hat{E}^{(+)}(\mathbf{r}_1,t_1)|\Psi\rangle_m = \frac{Z_m}{r_{m1}r_{m2}}e^{i(\mathbf{k}_c+\mathbf{k}_p)\cdot\mathbf{r}_m} \tag{1}$$

$$Z_m = i\mathcal{C}_{12}e^{-i\nu\tau_{m1}}e^{-i\omega\tau_{m2}}e^{-(\Gamma/2)\tau_{m1}} \times e^{-(\gamma/4)(\tau_{m2}-\tau_{m1})}\sin\tilde{\Omega}(\tau_{m2}-\tau_{m1}), \tag{2}$$

where $(\mathbf{k}_c + \mathbf{k}_p)\cdot\mathbf{r}_m$ is the coherent phase factor (CPF), $\Gamma = \gamma(\Omega_p/\Delta)^2$ is the Raman pumping rate, $\tilde{\Omega} = \sqrt{\Omega_c^2 - (\gamma/4)^2}$ is the effective Rabi frequency, $|\Psi\rangle_m = \sum_{\mathbf{kq}} C_{m\mathbf{kq}}(\infty)|c_m,1_{\mathbf{k}},1_{\mathbf{q}}\rangle$ is the two-photon state with $C_{m\mathbf{kq}}$ being the coefficient of the ground state c with one Stokes and one anti-Stokes photon, $\tau_{mj} = t_j - r_{mj}/c$ are emission times, $r_{mj} = |\mathbf{r}_m - \mathbf{r}_j|$ with $\tau_{m2} - \tau_{m1} > 0$ and $\mathcal{C}_{12} = -\frac{\Omega_p\Omega_c}{\tilde{\Omega}\Delta}\wp_{ba}\wp_{ca}(\frac{\omega\nu}{4\pi\varepsilon_o c^2})^2$ with $\wp_{\alpha\beta}$ the dipole transition matrix elements, and $\hat{E}^{(+)}(\mathbf{r}_j,t_j) = \sum_{\mathbf{k}}(\hat{\epsilon}_j\cdot\hat{\varepsilon}_{\mathbf{k}})\sqrt{\frac{\hbar\nu_{\mathbf{k}}}{2\varepsilon_o V}}\hat{a}_{\mathbf{k}}e^{i(\mathbf{k}\cdot\mathbf{r}_j-\nu_{\mathbf{k}}t_j)}$ is the collective electric field operator at detector j (=1,2) due to the contributions of N arrayed emitters.

Since the emitters are identical, independent, and noninteracting, there is no correlation between the fields from different emitters. The collective state of all the particles is the sum over all the emitters, $|\Psi\rangle = \frac{1}{\sqrt{N}}\sum_m|\Psi\rangle_m = \frac{1}{\sqrt{N}}\sum_{m\mathbf{kq}} C_{m\mathbf{kq}}(\infty)|c_m,1_{\mathbf{k}},1_{\mathbf{q}}\rangle$. Thus, the two-photon amplitude for the many-atoms state becomes

$$\psi^{(2)} = \langle 0|\hat{E}^{(+)}(\mathbf{r}_2,t_2)\hat{E}^{(+)}(\mathbf{r}_1,t_1)|\Psi\rangle = \sum_m \psi_m^{(2)}(1,2) = \sum_m e^{i(\mathbf{k}_c+\mathbf{k}_p)\cdot\mathbf{r}_m}Z_m K_{1m}Q_{2m}, \tag{3}$$

where

$$K_{1m} = k\left[f(x_{1m}) - g(x_{1m})\tfrac{1}{2}\sin^2\alpha_{1m}\right], \tag{4}$$

$$Q_{2m} = q\left[f(y_{2m}) - g(y_{2m})\tfrac{1}{2}\sin^2\alpha_{2m}\right], \tag{5}$$

are exact expressions valid for the near field, with $f(x_{1m}) = \frac{1}{x_{1m}} + i\frac{1}{x_{1m}^2} - \frac{1}{x_{1m}^3}$, $g(x_{1m}) = \frac{1}{x_{1m}} + i\frac{3}{x_{1m}^2} - \frac{3}{x_{1m}^3}$, $x_{1m} = kr_{1m}$, and $\sin\alpha_{jm} = (x_m - X_j)/r_{jm}(j = 1,2)$. Similar expressions for $f(y_{2m})$ and $g(y_{2m})$, with $y_{2m} = qr_{2m}$.

The two-photon correlation can then be obtained from $G^{(2)} = |\psi^{(2)}|^2$ and Eq. (3), which is valid for arbitrary distances r_{jm}. In the far field, $K_{jm} \to \frac{1}{r_{jm}}$.

For rectangular geometry the CPF can be expressed as $\exp[i\theta_{m,x} + i\theta_{m,y}]$ where $\theta_{m,x} = (k_{cx} + k_{px})x_m$ and $\theta_{m,y} = (k_{cy} + k_{py})y_m$. For a two-dimensional (2D) arrayed system we can replace $x_m \to ma$ and $y_m \to nb$.

The correlation for the case of two atoms can be written analytically as

$$G^{(2)} = \frac{\mathcal{C}_{12}}{(r_1 r_2)^2} 2e^{-\Gamma\tau_1} e^{-\gamma\tau_{21}} \sin^2 \tilde{\Omega}\tau_{21} \times \{1 + \cos[\nu\Delta\tau_1 + \omega\Delta\tau_2 - (\mathbf{k}_c + \mathbf{k}_p)\cdot\Delta\mathbf{r}]\}, \quad (6)$$

with $\Delta\tau_j = \tau_j - \tau_j'$, $\tau_j = t_j - r_j/c$, $\tau_j' = t_j' - r_j'/c$, $\Delta\mathbf{r} = \mathbf{r} - \mathbf{r}'$ is the vector joining the two emitters, and r_j and r_j' are the distances between the two emitters to detector j (=1,2). Analysis of Eq. (6) without the CPF can be found in Refs. [19,21] in the context of quantum microscopy.

III. 1D ARRAY OF EMITTERS

We focus on a 1D phased array of quantum emitters [see Figs. 1(b) and 1(c)]. This structure can be realized by using a holographic optical lattice for atoms [22] or a microtrap array for ions [23] as regular trapping sites, as well as an array of quantum dots [24]. Correlated photon pairs have been produced by using quantum dot driven by two-photon absorption in cascade configuration [25]. For the optical trapping system it might be a challenge to create a large number of sites, with each site containing only one atom, although this has been demonstrated with seven atoms [26]. Certain sites may contain two or more atoms. In the case of quantum dots, the decoherence rate $\gamma(\sim 410^{12}\ \mathrm{s}^{-1})$ is typically 1000 times higher than in atoms, significantly reducing the correlation time. Thus, cooling down to a few Kelvins is required. Quantum dots are usually grown at random locations. Recently, a large array of regularly spaced quantum dots has been produced by ion-beam irradiation [27].

Using $\mathbf{r}_m = md\hat{x}$, the amplitude goes as (since $t_i \simeq t_i'$)

$$\psi^{(2)} \simeq i\mathcal{C}_{12} e^{-i\nu t_1} e^{-i\omega t_2} \sum_m e^{-(\Gamma/2-\gamma/4)\tau_{m1}} e^{-(\gamma/4)\tau_{m2}} \times \frac{e^{imKd}}{r_{1m} r_{2m}} \exp[i(\nu r_{1m} + \omega r_{2m})/c] \times \sin\tilde{\Omega}\left(\tau + \frac{r_{1m} - r_{2m}}{c}\right), \quad (7)$$

where $-(N-1)/2 < m < (N-1)/2$, $K = k_{cx} + k_{px}$ is the coherent wave vector, $\tau = t_2 - t_1$ is the effective delay, and $r_{jm} = \sqrt{D_j^2 + x_{jm}^2}$ (with $x_{jm} = X_j - md$ and $j = 1,2$ for the detectors).

In the following figures we have plotted normalized correlation $g^{(2)} = |\psi^{(2)}/\mathcal{C}_{12}|^2_{r_{1m},r_{2m}=1}$ by neglecting the decay factors, the overall phase factors, and the overall constant. We also set $r_{1m}, r_{2m} \to 1$ since it does not yield important physics. Figures 1(b) and 1(c) show two possible configurations of the array of particles with the corresponding plots of the $g^{(2)}$ for $X_{1,2} = X$, computed from Eq. (7). The correlation patterns show that the Talbot images are revived at $D = 2z_T = 2d^2/(\lambda/2)$ which is twice the usual Talbot length z_T, in contrast to that reported in Ref. [28]. Our result implies that the effective wavelength is $\lambda/2$, as expected, due to the coincident detection. In the subsequent analysis and results we focus on the configuration with the central emitter only, as in Fig. 1(b), where N is odd.

A. Paraxial approximation

In the paraxial regime, $D_j \gg |md - X_j|$ leads to the constraint,

$$D_{1,2} \gg |X_{\max} + Nd|, \text{ constraint Ia.} \quad (8)$$

Substituting $\sqrt{D^2 + x^2}$ by $D + \frac{x^2}{2D} - \frac{x^4}{8D^3}$ in Eq. (7) and neglecting the quartic and higher order terms, we have

$$\psi^{(2)} \propto \sum_m \frac{e^{imKd}}{r_{1m} r_{2m}} \sin\tilde{\Omega}\left(\tau + \frac{1}{c}\left(\Delta D + \frac{x_{1m}^2}{2D_1} - \frac{x_{2m}^2}{2D_2}\right)\right) \times \exp\left\{i\left[\frac{\nu}{c}\left(D_1 + \frac{x_{1m}^2}{2D_1}\right) + \frac{\omega}{c}\left(D_2 + \frac{x_{2m}^2}{2D_2}\right)\right]\right\}, \quad (9)$$

where $\Delta D = D_1 - D_2$.

At the center $X_j = 0$, the negligible term $\frac{x^4}{8D^3}$ in paraxial approximation implies $\max\{\frac{(\nu+\omega)}{c}\frac{(md)^4}{8D^3} \simeq \frac{\pi}{\lambda}\frac{(md)^4}{2D^3}\} \ll 2\pi$. Taking $m \to N(\gg 1)$ we have the condition,

$$k\frac{(Nd)^4}{8\pi D^3} = \frac{(Nd)^4}{4\lambda D^3} \ll 1, \text{ constraint Ib.} \quad (10)$$

When $D = \frac{d^2}{\lambda}$ (in the order of the Talbot length) is substituted into Eq. (10), we have the constraint,

$$d > \frac{\lambda}{2} N^2 \text{ constraint II.} \quad (11)$$

B. Central amplitude

At the center $X_j = 0$ the amplitude Eq. (7) gives

$$\psi^{(2)}(0) \propto \sum_m \sin\tilde{\Omega}\left(\tau + \frac{r_{1m}^0 - r_{2m}^0}{c}\right) \times \frac{e^{imKd}}{r_{1m} r_{2m}} \exp\left[i\left(\nu r_{1m}^0 + \omega r_{2m}^0\right)/c\right], \quad (12)$$

where $r_{jm}^0 = \sqrt{D_j^2 + (md)^2}$. The paraxial approximation reduces Eq. (12) to

$$\psi^{(2)}(0) \propto e^{i(\nu D_1 + \omega D_2)/c} \sin\tilde{\Omega}\left(\tau + \frac{\Delta D}{c}\right) \times \sum_m \frac{e^{imKd}}{r_{1m} r_{2m}} \exp[iSm^2 d^2], \quad (13)$$

where $S = \frac{\nu/D_1 + \omega/D_2}{2c}$. The quadratic dependence in $e^{iSm^2d^2}$ is the consequence of the Fresnel (near-field) diffraction. The series summation gives the usual Talbot effect. For convenience, we give a short review and tutorial on the Talbot effect in the Appendix.

Letting $\nu/D_1 \simeq \omega/D_2$ ($S \simeq \frac{2\pi}{D\lambda}$) the central amplitude becomes $\psi^{(2)}(0) \propto \sum_m \exp[i\frac{2\pi}{D\lambda}m^2 d^2] = \sum_m \exp[i\pi m^2 \frac{z_T}{D}]$. When $D = z_T = \frac{2d^2}{\lambda}$, the series is a sum of equal numbers of terms with even and odd multiples of π for the case with central emitter [Fig. 1(b)], that is, $\sum_{m=-(N-1)/2}^{(N-1)/2} \exp[i\pi m^2] = 1 + 2(e^{i\pi} + e^{i4\pi} + e^{i9\pi} + e^{i16\pi}\ldots) = 1$ (N odd), giving $\psi^{(2)}(0) \simeq 1\,(\ll N)$ with almost no signal due to destructive interference of photons from all emitters except the central one. However, for the case with side emitters

[Fig. 1(c)], $\sum_{m=-(N-1)/2}^{(N-1)/2} \exp[i\pi m^2] = 2(e^{i\pi/4} + e^{i9\pi/4} + e^{i25\pi/4} + e^{i49\pi/4} + e^{i81\pi/4} + \cdots)$ (N even) would give a finite value.

IV. TWO-PHOTON DETECTION SCHEMES

The use of two detectors for obtaining the two-photon correlation provides a new method for acquiring information or signals, utilizing the novel properties of coherently phased nonclassical photon pairs with interference and diffraction effects.

A. Coincident detection

For detectors that coincide, $X_{1,2} = X$, Eq. (9) becomes (neglect the damping terms)

$$\psi^{(2)} \propto e^{i(\nu D_1 + \omega D_2)/c} \sum_m \frac{e^{imKd}}{r_{1m} r_{2m}} e^{iS(X-md)^2} \times \sin\tilde{\Omega}\left[\tau + \frac{\Delta D}{c}\left(1 - \frac{(X-md)^2}{2D_1 D_2}\right)\right], \tag{14}$$

where $S = \frac{\nu/D_1 + \omega/D_2}{2c}$, $\Delta D = D_1 - D_2$.

The Talbot effect is applicable for the region of X satisfying the constraint Eq. (8). Since $\frac{(X-md)^2}{D_1 D_2} \ll 1$, the final (quadratic) term in the sine function is much smaller than the second term and may be neglected, Eq. (14) becomes

$$\psi^{(2)} \propto \sin\tilde{\Omega}\left(\tau + \frac{\Delta D}{c}\right) \sum_m \frac{e^{imKd}}{r_{1m} r_{2m}} e^{iS(X-md)^2}, \tag{15}$$

where we have discarded the overall phase factor $e^{i(\nu D_1 + \omega D_2)/c}$ which gives no important effect. Thus, the nonclassical sine term does not depend on X within the Talbot region. For large X (i.e., beyond the paraxial region), however, the nonclassical effect would have X dependence. Assuming $\nu = \omega$ and taking $D_2 = \alpha D_1$ with $D_1 = D$ we have $\Delta D = (1-\alpha)D$, $S = \frac{\pi(1+\alpha^{-1})}{D\lambda}$, and

$$\psi^{(2)} \propto \sin\tilde{\Omega}\left(\tau + \frac{(1-\alpha)D}{c}\right) \times \sum_m \frac{e^{imKd}}{r_{1m} r_{2m}} \exp\left[i\frac{\pi(1+\alpha^{-1})}{D\lambda}(X-md)^2\right]. \tag{16}$$

The term with quadratic m is important for small D while the sine term is due to quantum interference. The CPF e^{imKd} gives the usual diffraction grating effect. It also has an effect of shifting the entire carpet along X.

Based on the constraint, Eq. (11), the analytical formula Eq. (16) in the paraxial regime gives results (shown in Fig. 2) that agree with the exact formula Eq. (7).

B. Symmetric detection

For detectors situated on symmetrically opposite locations $X_1 = -X$ and $X_2 = X$, Eq. (9) reduces to

$$\psi^{(2)} \propto \sum_m \frac{e^{imKd}}{r_{1m} r_{2m}} \exp\left[\frac{i}{2c}\left(\frac{\nu}{D_1} X_m^{(+)2} + \frac{\omega}{D_2} X_m^{(-)2}\right)\right] \times \sin\tilde{\Omega}\left[\tau + \frac{\Delta D}{c} + \frac{1}{2c}\left(\frac{X_m^{(+)2}}{D_1} - \frac{X_m^{(-)2}}{D_2}\right)\right], \tag{17}$$

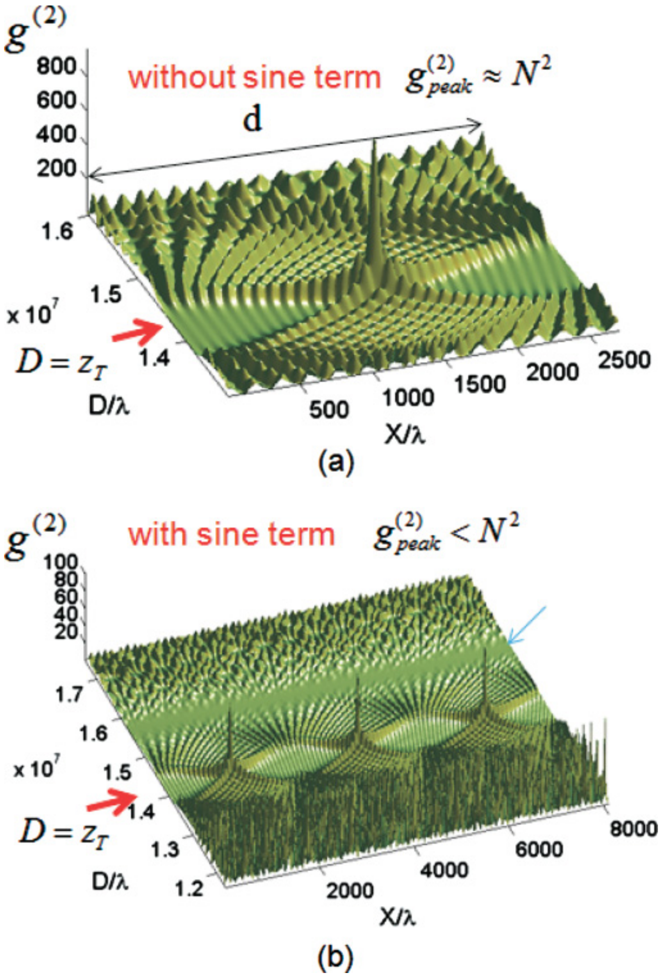

FIG. 2. (Color online) Two-photon correlation $g^{(2)}$ (normalized) plotted using Eq. (16) (for paraxial region) against $X = X_1 = X_2$ and $D = D_1$ at around $D = z_T$. Note that the images at $D = z_T$ [thick (red) arrow] are shifted half-period compared to the images at $D = 2z_T$ in Figs. 1(b) and 1(c). (a) Without the sine term showing peak intensity $g^{(2)}_{\max} = N^2 \simeq 900$ ($N \simeq 30$) and (b) with the sine term, corresponds to nonclassical Talbot carpet. The heights of the peaks at Talbot length $z_T = 2d^2/\lambda$ are below N^2 due to modulation by the sine term, due to quantum interference. The zero intensity channel [thin (blue) arrow] in (b) is independent of X. It occurs at the location $D_0 = \pi c/|1-\alpha|\tilde{\Omega}$ ($\alpha = 1.001$) (i.e., inversely proportional to the effective Rabi frequency $\tilde{\Omega}$). We use $N = 31$, $\Omega_c = 2000\Gamma$, $D_2 = 1.001 D_1$, and $d = 3N^2\lambda$.

where $X_m^{(\pm)} = X \pm md$. Simpler expression is obtained by letting $D_1 = D_2$ and $\nu = \omega$,

$$\psi^{(2)} \propto \sum_m \frac{e^{imKd}}{r_{1m} r_{2m}} e^{i\frac{2\pi m^2 d^2}{\lambda D}} \sin\tilde{\Omega}\left(\tau + \frac{2Xmd}{Dc}\right). \tag{18}$$

At $D = z_T/2 = \frac{d^2}{\lambda}$ the amplitude takes the form $\sum_{m=-N}^{N} \sin\tilde{\Omega}(\tau + m\frac{\lambda X}{cd})$, which vanishes at $X = 0$ when $\tau = 0$.

The dependency on X is governed by the nonclassical sine (interference) function. Both the argument in the sine function and the coherent phase factor depend linearly on m. We see that the X dependence is important when $\frac{2\pi Nd}{\lambda} \sim \tilde{\Omega}\frac{X}{c}$ or Nd is not too large. The relative magnitudes of the terms are,

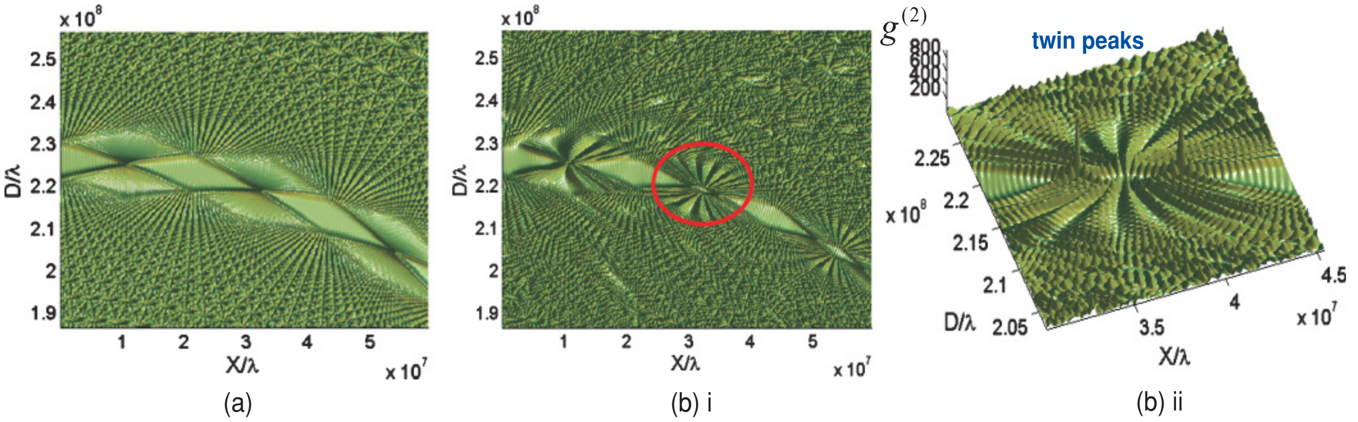

FIG. 3. (Color online) Two-photon correlation $g^{(2)}$ (top view) beyond paraxial approximation for opposite detectors ($X_2 = -X_1 = X$) [plotted using the exact expression and not the paraxial Eq. (18)] for: (a) without the sine term and (b) with the sine term, where (ii) is the magnified view of the circled area in (i). Note that the peaks and regions of destructive interference now depend on X. The scale along X is substantially larger than the $X_2 = X_1$ case (i.e., $X_{\max} = 5500d$. Here, $N = 61$ with other parameters $\Omega_c = 2000\Gamma$, $D_2 = 1.001D_1$, and $d = 3N^2\lambda$, the same as in Fig. 2.

$mKd : \frac{2\pi m^2 d^2}{\lambda D} : \tilde{\Omega} m d \frac{2X}{Dc} = 1 : \frac{Nd}{D} : \frac{\tilde{\Omega}}{\nu}\frac{X}{D}$. Taking into account $d \sim \lambda N^2$ and $D \sim d^2/\lambda \sim \lambda N^4$ we have $1 : \frac{1}{N} : \frac{\tilde{\Omega}}{\nu N}\frac{X}{Nd}$.

In Fig. 3 we plot Eq. (7), the exact expression for $G^{(2)}$ (beyond paraxial region). Here, the scale along X has to be larger than the scale in Fig. 2 by a factor of $N\nu/\tilde{\Omega}$ in order to see the nonclassical pattern. Figure 3(a) shows how the two detectors at the opposite sides of the y axis can produce such a *distorted* Talbot pattern. The main feature here is the arc structure, which is mainly due to the departure from the paraxial region. The peaks of the structure vary with both D and X, even without the sine term. The presence of the nonclassical sine term makes the pattern less regular with more complicated features [see Fig. 3(bi)]. A closer look reveals a prominent twin-peaks feature, as shown in Fig. 3(bii). Further studies and analysis of this structure are required to gain insights for new applications.

V. DISCUSSIONS

We elaborate on several important aspects of the results, particularly for generating nonclassical light sources with high intensity and the significance of the nonclassical interference "sine" term on the spatial structure of the nonclassical Talbot pattern.

A. Toward intense nonclassical light

Figure 2(a) shows the coherence effect of the two-photon correlation (i.e., the peak intensity of $G^{(2)}$ scales with N^2, regardless of whether the coherent phase factor $\exp[imKd]$ is present). The result shows that the coherent method can produce high-intensity photon pairs without using the nonlinear amplification process. If we let $d = 10\lambda$, large enough for the neglect of dipole-dipole interaction, with $\lambda = 300$ nm, an array size of 3 cm would contain 10^4 emitters which provide $N = 10^8$ photons in one collective emission corresponding to an energy of $U = N\hbar\nu \sim 7 \times 10^{-11}$ J. The cyclic pumping duration corresponds to the spontaneous emission lifetime $1/\Gamma \sim 10^{-8}$ s. Thus, the power is $P = U\Gamma = 7$ mW. The width of the peaks is about 50λ, thus the intensity is $I = P/\sigma \sim 10^7$ Wm^{-2}, which is close to the intensity of a typical diode laser with 100-mW power, diameter of 5 mm. This result shows that it is possible to engineer a coherent source of nonclassical light with high intensity by constructing arrayed emitters that are coherently phased, providing the prospect for generation of intense nonclassical light, providing a coherent amplification method for two-photon lithography compared to existing parametric amplification schemes using an optical parametric amplifier (OPA) [29], an optical parametric oscillator (OPO) [30], and an image-forming projection system using the optical transfer function [31].

B. Laser-controlled Talbot effect

The nonclassical sine term modulates the entire Talbot pattern in Fig. 2(b), lowering the peak intensity below N^2 level. It gives the no-signal (NS) channel as the result of destructive interference at all values of X. This happens (for $\tau = 0$) at D_1 satisfying $\tilde{\Omega}\frac{|1-\alpha|D_1}{c} = m\pi$, m is integer. The spatial period between two NS lines is

$$D_0 = c\pi/(\tilde{\Omega}|1-\alpha|), \qquad (19)$$

which correctly gives the location of the destructive interference in Fig. 2(b).

This feature gives a useful laser-controlled Talbot effect. The Talbot image at a specific location of D_{image} can be erased by tuning the control field (through $\tilde{\Omega}$) such that $D_{\text{image}} = mD_0$. We also find the coherent phase factor (CPF) has an effect of shifting the entire pattern horizontally, across X. This provides another coherent control mechanism in another dimension.

Since the resulting (modulated) two-photon Talbot pattern contains essentially the same old features as the classical case, it should be applicable for mode locking and factorization of numbers using two-photon light sources. Moreover, the laser-controlled Talbot effect can be developed into an innovative system of dynamically controlled phase locking.

C. Other features

In addition to the main features discussed above, there are a few side points to note. On closer inspection of the Talbot patterns in Figs. 2 and 3, we find seemingly chaotic and irregular background oscillations which look like sea waves around regularly revived peaks (images of the source). This peculiar feature may provide insight in connection with the formation of rogue waves [32]. Also, in the near field ($kr_{1m},qr_{2m} \sim 1$), the N^2 dependence does not apply and we find no Talbot effect. Finally, the coherent phase factor (due to lasers) introduces an overall shift that has little effect on the general features.

VI. CONCLUSIONS

The present work shows that a coherently phased array of quantum emitters can produce large number of correlated photon pairs that scales with N^2 at localized spots, with promising intensity close to a diode laser. This is a significant step forward to realizing new kinds of light sources with high intensity and nonclassical properties which could lead to new possibilities, particularly in quantum nonlinear optics with intense nonclassical light.

We have also studied the spatial structures of the two-photon correlation function $G^{(2)}$ for the 1D array of nonclassical emitters with two detectors. When the detectors coincide, $X_1 = X_2$, the $G^{(2)}$ distribution across the screen position X and distance D displays patterns reminiscent of the classical Talbot carpet, but with effective Talbot length twice the classical Talbot length. The nonclassical interference "sine term" provides a possibility to tune the intensity of the Talbot image by using the control laser. However, when the detectors are on the opposite sides of the y axis, such that $X_1 = -X_2$, we find unique structure in the $G^{(2)}$ as the result of the two-detector scheme, which is not present in the single-photon detection case. The structure varies over a larger scale, beyond the paraxial region and displays a distorted Talbot pattern. The most interesting result is the effect of the interference "sine term," which makes the pattern more intricate and complex. Our results on the nonclassical version of the two-photon Talbot effect could be useful for the development of nonclassical optics and diffractive optical elements based on nonclassical light sources.

ACKNOWLEDGMENTS

This work is supported by University of Malaya Research Grant No. RG111/10AFR. C. H. R. Ooi and B. L. Lan thank Monash University for support through the internal research fund.

APPENDIX: TALBOT EFFECT

The self-images of the original periodic structure would appear at multiples of a distance $z_T = \frac{2d^2}{\lambda}$, called the Talbot length. The same pattern would also recur at $D = (2n + 1)z_T/2$, but shifted in space by half the spatial period. Higher order fractional revivals occur at rational multiples of z_T.

At $D = (p/2)z_T/q$ (particularly $z_T/4$, $3z_T/4, \ldots,$ $z_T/6$, $3z_T/6$, $5z_T/6, \ldots z_T/8$, $3z_T/8$, $5z_T/8$, $7z_T/8, \ldots$) with $q = 1,2,3,\ldots$; $p = 1,3,5\ldots$, the images would recur but they are inverted or shifted in space by half-period, each consists of q copies of the original grating, separated by d/q.

At $D = rz_T/s$ (particularly $z_T/3, 2z_T/3, \ldots, z_T/5, 2z_T/5$, $3z_T/5$, $4z_T/5, \ldots$) with $s = 3, 5, 7\ldots$; $r = 1, 2, 3\ldots$, the images are *not* shifted, but each consists of s copies of the original grating, separated by d/s.

---

[1] M. D'Angelo, M. V. Chekhova, and Y. Shih, Phys. Rev. Lett. **87**, 013602 (2001).

[2] Y. Shih, J. Mod. Opt. **49**, 2275 (2002).

[3] M. O. Scully, U. W. Rathe, C. Su, and G. S. Agarwal, Opt. Commun. **136**, 39 (1997).

[4] M. O. Scully and K. Druhl, Phys. Rev. A **25**, 2208 (1982).

[5] C. H. Raymond Ooi, Phys. Rev. A **75**, 043817 (2007).

[6] C. H. Raymond Ooi, Q. Sun, M. S. Zubairy, and M. O. Scully, Phys. Rev. A **75**, 013820 (2007).

[7] V. Balic, D. A. Braje, P. Kolchin, G. Y. Yin, and S. E. Harris, Phys. Rev. Lett. **94**, 183601 (2005).

[8] X. Li, J. Chen, P. l Voss, J. Sharping, and P. Kumar, Opt. Express **12**, 3737 (2004); J. Fulconis, O. Alibart, W. J. Wadsworth, P. St. J. Russell, and J. G. Rarity, *ibid.* **13**, 7572 (2005).

[9] Q. Lin, F. Yaman, and G. P. Agrawal, Phys. Rev. A **75**, 023803 (2007); Opt. Lett. **31**, 1286 (2006).

[10] S. E. Harris, Phys. Rev. Lett. **98**, 063602 (2007).

[11] C. H. Raymond Ooi, J. Appl. Phys. **107**, 043110 (2010).

[12] W. H. F. Talbot, *Facts Related to Optical Science, No. IV*, Philos. Mag. **9**, 401 (1836).

[13] R. Iwanow *et al.*, Phys. Rev. Lett. **95**, 053902 (2005).

[14] O. M. Friesch, I. Marzoli, and W. P. Schleich, New J. Phys. **2**, 4 (2000).

[15] A. E. Kaplan, P. Stifter, K. A. H. van Leeuwen, W. E. Lamb Jr., and W. P. Schleich, Phys. Scr. T **76**, 93 (1998); A. E. Kaplan, I. Marzoli, W. E. Lamb Jr., and W. P. Schleich, Phys. Rev. A **61**, 032101 (2000).

[16] J. R. Leger, Appl. Phys. Lett. **55**, 334 (1989); Y. Kono *et al.*, IEEE J. Quantum Electron. **36**, 607 (2000).

[17] D. Bigourd, B. Chatel, W. Schleich, and B. Girard, Phys. Rev. Lett. **100**, 030202 (2005).

[18] C. H. Raymond Ooi, Phys. Rev. A **75**, 043817 (2007); C. H. Raymond Ooi, B.-G. Kim, and H.-W. Lee, *ibid.* **75**, 063801 (2007).

[19] M. O. Scully and C. H. Raymond Ooi, J. Opt. B: Quantum Semiclass. Opt. **6**, S816 (2004).

[20] C. H. Raymond Ooi, A. K. Patnaik, and M. O. Scully, *Noise and Information in Nanoelectronics, Sensors, and Standards III*, in Proceedings of the SPIE **5846**, 1, Bellingham, Washington (The International Society for Optical Engineering, Bellingham, 2005).

[21] M. O. Scully, Concepts of Physics **2**, 261 (2005).

[22] S. Bergamini, B. Darquié, M. Jones, L. Jacubowiez, A. Browaeys, and P. Grangier, J. Opt. Soc. Am. B **21**, 1889 (2004).

[23] J. Chiaverini and W. E. Lybarger Jr., Phys. Rev. A **77**, 022324 (2008).

[24] Q. Sun *et al.*, Nature Photonics **1**, 717 (2007).

[25] C. Santori, D. Fattal, J. Vuckovic, G. S. Solomon, and Y. Yamamoto, Fortschr. Phys. **52**, 1180 (2004).

[26] D. G. Grier, Nature **424**, 810 (2003).

[27] M. Buljan *et al.*, Phys. Rev. B **81**, 085321 (2010).

[28] K. H. Luo *et al.*, Phys. Rev. A **80**, 043820 (2009).

[29] G. S. Agarwal *et al.*, J. Opt. Soc. Am. B **24**, 270 (2007).

[30] H. Cable, R. Vyas, S. Singh, and J. P. Dowling, New J. Phys. **11**, 113055 (2009).

[31] N. Fukutake, J. Mod. Opt. **53**, 719 (2006).

[32] N. Akhmediev, J. M. Soto-Crespo, and A. Ankiewicz, Phys. Rev. A **80**, 043818 (2009).